Restratification at a California Current Upwelling Front. Part II: Dynamics

LEAH JOHNSON

Brown University, Providence, Rhode Island

CRAIG M. LEE AND ERIC A. D'ASARO

Applied Physics Laboratory, Seattle, Washington

JACOB O. WENEGRAT[a] AND LEIF N. THOMAS

Stanford University, Stanford, California

ABSTRACT

A coordinated multiplatform campaign collected detailed measurements of a restratifying surface intensified upwelling front within the California Current System. A companion paper outlined the evolution of the front, revealing the importance of lateral advection at tilting isopycnals and increasing stratification in the surface boundary layer with a buoyancy flux equivalent to $2000 \, \mathrm{W \, m^{-2}}$. Here, observations were compared with idealized models to explore the dynamics contributing to the stratification. A 2D model combined with a reduced form of the horizontal momentum equations highlight the importance of transient Ekman dynamics, turbulence, and thermal wind imbalance at modulating shear in the boundary layer. Specifically, unsteady frictional adjustment to the rapid decrease in wind stress created vertically sheared currents that advected horizontal gradients to increase vertical stratification on superinertial time scales. The magnitude of stratification depended on the strength of the horizontal buoyancy gradient. This enhanced stratification due to horizontal advection inhibited nighttime mixing that would have otherwise eroded stratification from the diurnal warm layer. This underscores the importance of near-surface lateral restratification for the upper ocean buoyancy budget on diel time scales.

1. Introduction

In regions with strong lateral density contrasts, density fronts can slump, transforming horizontal buoyancy gradients into vertical stratification on time scales that compete with surface forcing variability. The surface ocean is populated with fronts ranging in size from mesoscale $O(10–100)$ km to submesoscale $O(0.1–10)$ km (Rudnick 1999; Hosegood et al. 2006; Mahadevan et al. 2012; Thompson et al. 2016), which have cumulative impacts on basin scale stratification, surface potential vorticity (PV) and the distribution of heat, salt, and biogeochemical tracers within the upper ocean (Su et al. 2018; Lévy et al. 2010; Fox-Kemper et al. 2011; Wenegrat et al. 2018). A global analysis suggests that frontal processes are responsible for enhanced stratification in the upper oceans during the transition into spring (Johnson et al. 2016) and direct observations of frontal slumping reveal the importance of horizontal gradients on the upper ocean buoyancy budget in different regions [e.g., North Pacific Ocean (Hosegood et al. 2006), Arctic (Timmermans and Winsor 2013), and Oregon coast (Dale et al. 2008)]. Yet the dominant dynamical processes responsible for the rearrangement of buoyancy at fronts remains elusive as interpreting direct observations of frontal slumping are challenging due to the time–space aliasing inherent in surveying such rapidly evolving features. Observations that can help elucidate the dynamics leading to stratification at upper ocean fronts are essential for identifying the role of horizontal buoyancy gradients on the momentum and buoyancy budget of the upper ocean.

ᵃ Denotes content that is immediately available upon publication as open access.

ᵃ Current affiliation: University of Maryland, College Park, College Park, Maryland.

Corresponding author: Leah Johnson, leah_johnson@brown.edu

A set of observations reported in Johnson et al. (2020, hereinafter Part I) described a Lagrangian view of a stratifying submesoscale front in the California Current System. The frontal evolution was divided into three stages: stage 1, downfront winds and turbulent mixing in the boundary layer (BL); stage 2, diurnal warming and frontal slumping; and stage 3, nighttime surface cooling and winds, and rapid near-surface stratification. This paper aims to describe the dynamics responsible for the rapid restratification by incorporating numerical models alongside the observational analysis described in Part I. Analyses in Part I showed that the observed stratification was due to lateral advection of the cross-frontal gradients by vertically sheared horizontal currents. The main focus of the modeling here is to understand the dynamics of these currents.

The hydrostatic equation for horizontal momentum can be written

$$\frac{D\mathbf{u}_h}{Dt} = -f\hat{z} \times \mathbf{u}_h - \frac{1}{\rho_o}\nabla p + \frac{\partial}{\partial z}\left(\nu\frac{\partial \mathbf{u}_h}{\partial z}\right), \qquad (1)$$

where f is the Coriolis parameter, ν is the turbulent eddy viscosity associated with the boundary layer, and p is the reduced pressure.

The vertical derivative of Eq. (1) was adopted to focus on vertical shear, yielding

$$\frac{\partial}{\partial t}\frac{\partial u}{\partial z} = f\frac{\partial v}{\partial z} - \frac{\partial b}{\partial x} + \frac{\partial^2}{\partial z^2}\left(\nu\frac{\partial u}{\partial z}\right) \quad \text{and} \qquad (2)$$

$$\frac{\partial}{\partial t}\frac{\partial v}{\partial z} = -f\frac{\partial u}{\partial z} - \frac{\partial b}{\partial y} + \frac{\partial^2}{\partial z^2}\left(\nu\frac{\partial v}{\partial z}\right), \qquad (3)$$

where the advective terms were ignored and the pressure term was replaced with density using the hydrostatic approximation $\partial p/\partial z = -g\rho$ and buoyancy $b = -g\rho/\rho_o$. This system of equations was combined into one in complex form assuming $Y = \partial u/\partial z + i\partial v/\partial z$ and $M^2 = \partial b/\partial x + i\partial b/\partial y$:

$$\frac{\partial}{\partial t}Y = -ifY \;-\; M^2 + \frac{\partial^2}{\partial z^2}(\nu Y)$$

$$\text{(TEND) (CORI) (PRES) (DIFF)} \qquad (4)$$

describing the shear tendency (TEND) resulting from the inertial term (CORI), the pressure gradient (PRES), and friction (DIFF). The boundary conditions were

$$\nu Y = \frac{1}{\rho}T \quad \text{at} \quad z = 0, \quad \nu Y = 0 \quad \text{at} \quad z = -H, \qquad (5)$$

where H is the mixed layer depth and $T = \tau^x + i\tau^y$ is the complex wind stress at the surface.

Note the combination of balances encapsulated in Eq. (4): TEND and CORI capture internal waves with

frequency set at Earth's rotation. The evolution of TEND, CORI, and PRES were explored by Tandon and Garrett (1994, hereinafter TG94) in an inviscid frontal adjustment of nearly vertical isopycnals at rest. TEND, CORI, and DIFF is the time-dependent Ekman problem (McWilliams and Huckle 2006; Wenegrat and McPhaden 2016) and when integrated vertically becomes the slab ML model of wind-driven near-inertial oscillations (NIO; Pollard and Millard 1970). CORI + PRES is thermal wind balance, and adding DIFF becomes turbulent thermal wind (TTW; Gula et al. 2014; McWilliams et al. 2015), also known as the generalized Ekman model (Cronin and Kessler 2009; Wenegrat and McPhaden 2016). It will be shown that each of these balances alone are insufficient to describe the observations, yet when combined, work to create a shear tendency capable of tilting isopycnals and enhancing stratification comparable with the observations in Part I.

Dauhajre and McWilliams (2018) employed a framework similar to Eq. (4) to investigate the diurnal cycle on a wind forced front. The results suggested a transition between two phases. Nighttime winds and cooling induced turbulent mixing and an overturning circulation as the front approached TTW balance. The onset of solar warming decreased turbulent fluxes, leaving a front out of thermal wind balance and in an unsteady state. This state resulted in an inertial response of the front akin to low level jets developed in the atmosphere (Van de Wiel et al. 2010). The system transitioned back toward a diffusive regime with the onset of nighttime cooling that damped the inertial oscillation and redeveloped a TTW circulation. Dauhajre and McWilliams (2018) explored the rectification of time dependence on classical TTW as a modified transient turbulent thermal wind (T3W). The observations in Part I describe a slightly different regime than the T3W problem in that there was a rapid decrease in convective and wind-driven turbulence as opposed to steady wind forcing. The implied response of the front to this rapid decrease in wind-driven mixing was an adjustment from a state of thermal wind imbalance set by nearly vertical isopycnals, ageostrophic shear and momentum flux divergence.

In section 3, a one dimensional model (1D) is used to show that the rapid appearance of stratification cannot be simulated by vertical mixing physics alone. In section 4, a two-dimensional (2D) model including turbulence viscosity and driven by the observed forcing heat flux and wind stress is used to simulate the response of the ocean. Because of the lack of frontogenesis in this model, the lateral gradients were an order of magnitude less than observed in Part I. Nevertheless, the 2D results can be accurately reproduced by solving Eq. (4) using the average turbulent viscosity (1D+), as shown in

section 4a. Furthermore, when nondimensionalized by balanced Richardson number Ri_b, 2D and 1D+ are shown to reproduce the observed increase in stratification (section 4b), signifying that the observed currents, and thus the restratification, is controlled by dynamics in the reduced set of equations represented by Eq. (4). The observations (OBS) contrasted with 1D, 2D, and 1D+ provide insight into the role of alongfront variability present in the observations as described in Part I.

2. Model setup and observations

The models employed here include Price–Weller–Pinkel (1D; Price et al. 1986), the MITgcm (2D; Marshall et al. 1997), and the reduced set of Eq. (4) (1D+). The models were forced and initialized with the observations. A hyperbolic tangent function was used to approximate the observed cross-frontal structure of T and S that sets the initial conditions for the models (see the appendix).

a. 1D setup

The 1D upper ocean response to the observed surface forcing was explored using the Price–Weller–Pinkel model (1D; Price et al. 1986), similar to that implemented in Farrar et al. (2007). The approximated cross-frontal structure (see the appendix) was horizontally averaged to produce a single initial profile of T and S. The model was run with 1-m vertical resolution and a 60-s time step. The time span began at the onset of winds [yearday (yd) 210, 6 days before the start of the survey], and the model was run for 8 days (when the survey ended).

b. 2D setup

The MITgcm (2D) was run in hydrostatic mode with a grid resolution of 300 m in the horizontal and 3 m in the vertical. The domain was horizontally periodic, with two fronts approximately 95 km apart. The configuration included two grid cells in the alongfront direction, for a total of 600 m. Details of the model setup can be found in the appendix. Changes in the alongfront direction are negligible, and therefore the model is considered 2D. The vertical extent was 0–150 m in depth. In this 2D configuration, northerly winds were exactly downfront and did not account for the curvature of the front, which modified the orientation between wind stress and horizontal buoyancy gradient relative to OBS. Results are presented in terms of alongfront (u^{af}, positive south in OBS) and cross front (u^{xf}, positive east in OBS). The model began with the onset of winds (yd 210, 6 days before the survey) which allowed for a comprehensive study of unsteady wind forcing on the front.

c. 1D+ setup

A reduced model (1D+) was evaluated by solving Eq. (4) numerically. The vertical derivatives were solved using a second-order finite difference discretization operator and then stepped forward with a Crank–Nicolson method, an implicit method for solving stiff ordinary differential equations (LeVeque 2007). Boundary conditions in Eq. (5) were included in the discretized operator in DIFF. The 1D+ model was solved at every grid point across the front in 2D, initialized with a profile of Y, ν, and M^2 from 2D at the time the observed float gets trapped near the surface (yd 216.3; stage 2). Profiles of ν and M^2 were set constant in time and the solution was integrated in z to obtain values for u^{af} and u^{xf} assuming no motion at the bottom. Solutions here were considered to be 1D because they were decoupled from neighboring grid points and therefore do not include frontogenesis or advection of momentum.

d. Observations

Model results were compared with a coordinated set of observations using a Lagrangian float and a ship-towed Triaxus profiling vehicle (details are in Part I). The observed and simulated front was surface intensified above a pycnocline at ~30 m. This near-surface layer will be referred to as the mixed layer (ML) for simplicity, though, consistent with many other studies, this layer was not always well mixed in momentum and buoyancy. A comparison between 1D, 2D, and OBS is in Fig. 1.

3. 1D: Surface buoyancy and momentum

In the absence of horizontal stratification, the upper ocean buoyancy budget responds to momentum and buoyancy fluxes at the surface. The observations spanned 30 h, capturing a cycle of nighttime mixing that bracketed daytime warming. This diurnal forcing imprinted buoyancy and momentum in the near-surface layers. Although the model was initiated 6 days prior to the survey, only results coinciding with the observations are discussed here.

In 1D, the onset of daytime warming along with decreased winds (stage 2) shoaled the once well mixed layer that persisted for several days of strong winds (i.e., prior to and during stage 1). During stage 2, the near-surface layer warmed, building stratification in the upper 3 m. The onset of winds and nighttime cooling (stage 3) simultaneously eroded the diurnal stratification and pushed it deeper into the water column, much like other models of the diurnal cycle (Price et al. 1986). At this time, the distribution of stratification in OBS
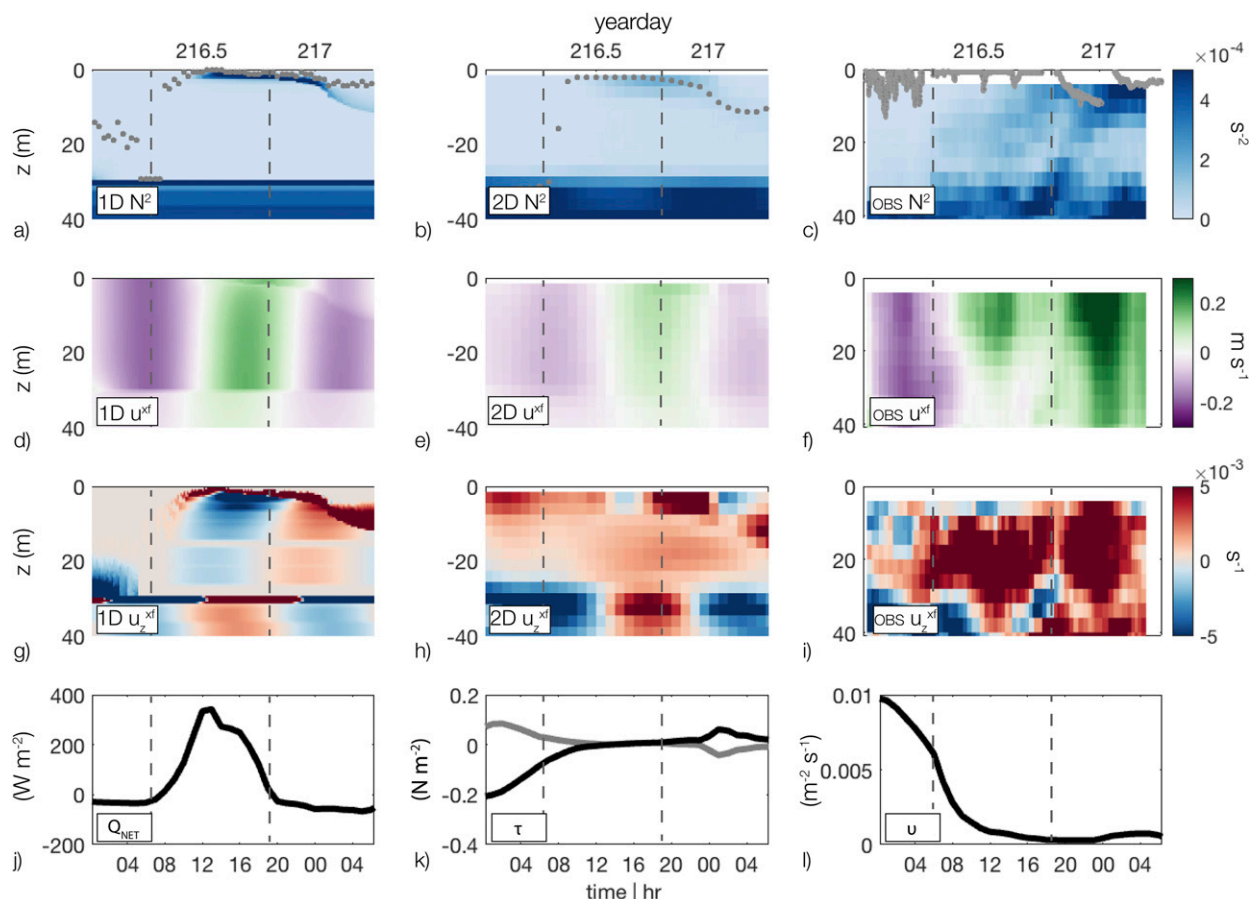
FIG. 1. The vertical structure of the ML for (left) 1D, (center) 2D, and (right) OBS for stratification [(a) 1D N^2 with Price–Weller–Pinkel ML (gray dots), (b) 2D N^2 with KPP boundary layer depth (gray dots), and (c) OBS N^2 with float depth (gray dots)], cross-frontal velocity [(d) 1D u^{xf}, (e) 2D u^{xf}, and (f) OBS u], and (g)–(i) cross-frontal shear [(g) 1D u_z^{xf}, (h) 2D u_z^{xf}, and (i) OBS u_z]. Also shown is the surface forcing used in 1D and 2D: (j) Q_{NET}, (k) τ^{af} (gray) and τ^{xf} (black), and (l) ML average viscosity ν. Vertical dashed lines separate the different stages 1–3 that are outlined in section 1.

deviated from the simple model (Fig. 1), as it increased throughout the ML (e.g., at 15 m, below the 1D ML) and was enhanced near the surface.

The difference in vertical gradients of T, S, and ρ from OBS and 1D highlights the importance of horizontal and vertical variability. During diurnal warming, the float was trapped at 2 m and therefore provided information near the surface (Fig. 2). In this near-surface layer, the float captured diurnal changes in N^2 and T_z similar to 1D. Yet, the increase in magnitude of S_z observed by the float in the absence of freshwater forcing suggests horizontal advection not captured by the 1D simulation. Additionally, Triaxus measured stratification deeper in the ML that was completely absent in 1D. This is evidence of warm freshwater sliding over the cold salty upwelled waters defining the front. The largest difference between 1D and OBS occurred at the onset of stage 3 as surface cooling and increased winds (yd 216.8) eroded the daytime stratification in 1D. In OBS, the

near-surface layer continued to stratify, resisting the tendency of surface forcing to erode near-surface stratification. This difference between 1D and OBS, with the large observed gradients in T and S, reveal the importance of lateral stratification on the upper ocean buoyancy budget.

Although 1D had some skill at capturing a thin diurnal warm layer observed by the float, it failed to capture the evolution of stratification deeper in the ML as well as the enhanced stratification during stage 3. In these cases, the salinity structure in the absence of freshwater forcing brings attention to key role of horizontal advection. The rest of this study considers lateral processes.

4. 2D: Friction, inertial motions, turbulent mixing

a. Adjustment and turbulence

The transient response of the front to unsteady winds in 2D is apparent in (Fig. 3), as Ekman transport from
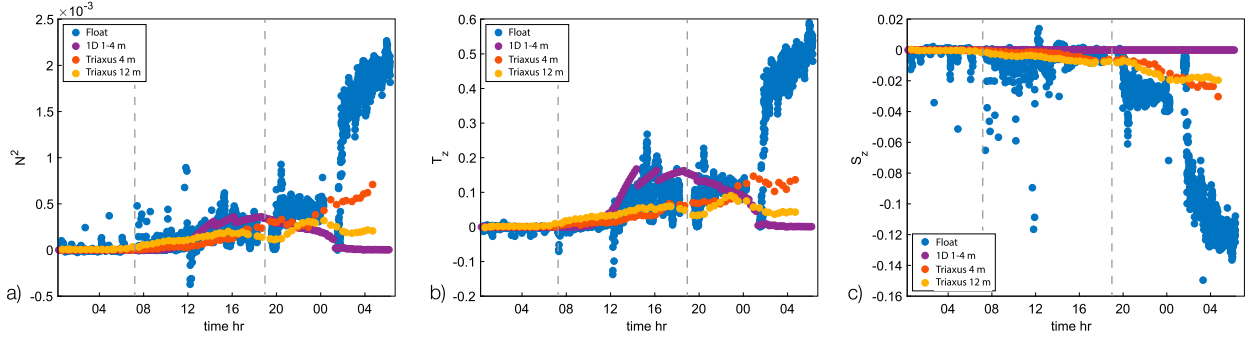
FIG. 2. Vertical gradients predicted by 1D (purple) compared with those observed by the float (blue), Triaxus at 4 m (orange), and Triaxus at 12 m. Variables include (a) b, (b) T, and (c) S. Vertical dashed lines separate the different stages 1–3 that are outlined in section 1.

downfront winds advected the front toward the warm (less dense) side of the front. As the winds subsided, both the modeled front and the observed front curved back toward the cold (dense) side of the front, and the modeled front continued to oscillate.

The oscillations in 2D can be described by an inertial response to wind forcing averaged throughout the ML (Pollard and Millard 1970):

$$\frac{du}{dt} - fv = \frac{\tau_x}{\rho_o H} \quad \text{and} \tag{6}$$

$$\frac{dv}{dt} + fu = \frac{\tau_y}{\rho_o H}. \tag{7}$$

Equations (6) and (7) were solved for the entire length of the model runs initialized when $\tau \approx 0$ assuming $u_i^{af} = u_i^{xf} = 0$, and $H = 30$ m (Figs. 3c–e). The solutions to Eqs. (6) and (7) agree well with 1D and 2D, suggesting the wavelike pattern after the winds subsided were wind-driven NIO. Similarly, in the observations, the float slowed (Fig. 3e) and turned eastward (Figs. 3b,c), albeit at a pace faster than the 2D model. The observations also exhibited higher-frequency oscillations not captured by NIO, suggesting alongfront variability associated with either physical meanders or superinertial motions along the front.

The persistent winds diffused the front in 2D, causing a weaker horizontal buoyancy gradient than observed
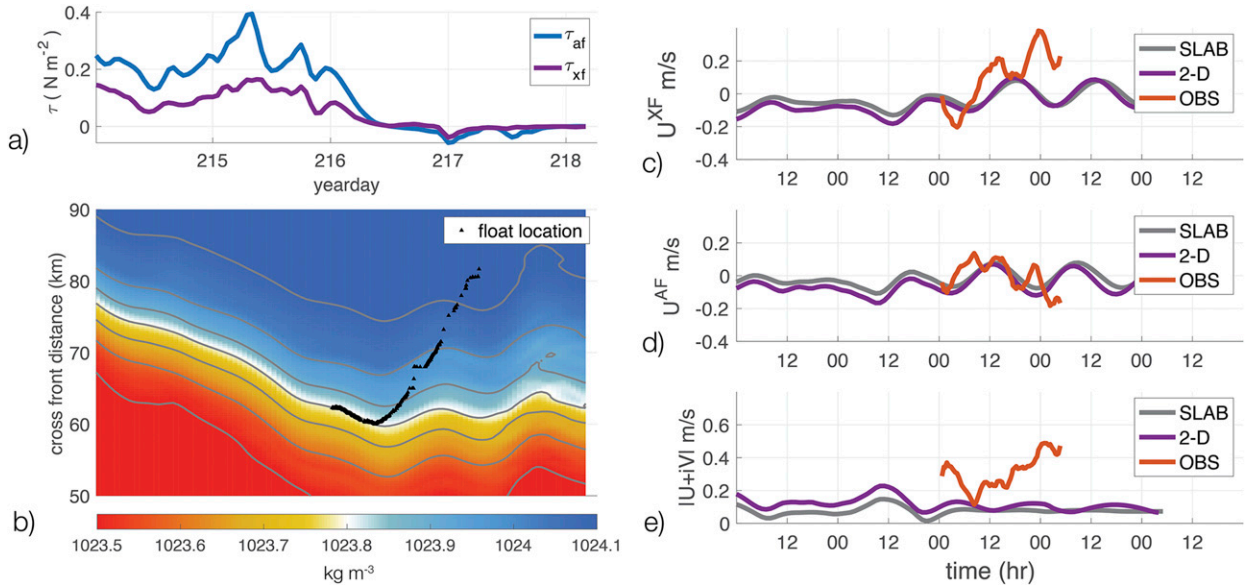

FIG. 3. NIO at the front as a response to a sudden decrease in winds: (a) Wind stress starting 3 days after the start of 2D and 2 days before the survey began; τ^{af} is blue, and τ^{xf} is purple. (b) Plan view of surface ρ in 2D as a function of cross-frontal distance and time. Gray lines are isopycnals, and black dots are the cross-frontal distance of the float trajectory overlaid for reference. Also shown is the surface velocity from 2D (purple), the solution to Eqs. (6) and (7) (gray), and OBS (orange) for (c) u^{xf} in models and u in OBS, (d) u^{af} and $-v$ in OBS, and (e) $|U|$ for model and OBS.
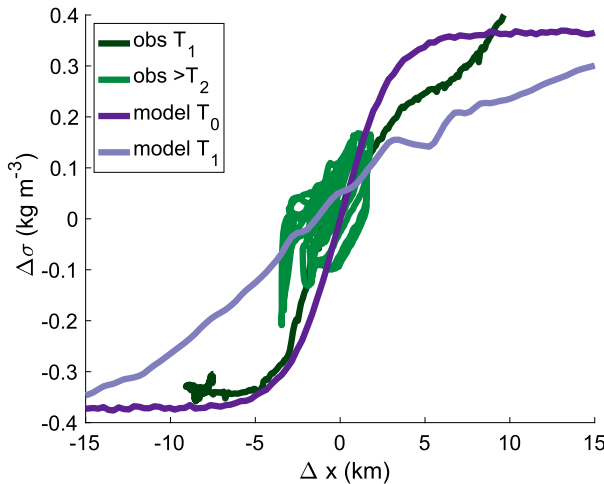
FIG. 4. Cross-frontal density structure from OBS compared with 2D. The initial Triaxus transect (obs T_1; dark green) crossed the entire front. Triaxus while following the float (obs $> T_2$; light green) surveyed the sharpest part of the front. Also shown are 2D after one time step, 6 days before OBS (model T_0; dark purple), and the cross-frontal structure in 2D at the start of the Lagrangian survey (model T_1; light purple) after 6 days of wind forcing.

FIG. 5. (a) Cross-frontal shear u_z^{xf} and (b) alongfront shear u_z^{af} in 2D (gray), 1D+ (purple), and OBS (orange). The contribution of the inertial terms CORI + PRES (red) and friction DIFF (teal) to the shear budget in 2D are also included.

(Fig. 4). The difference can be attributed to a lack of external strain in 2D compared to OBS (Part I). Nonetheless, the agreement between OBS and 2D as wind forcing decreased suggests an inertial response of the front. Although Eqs. (6) and (7) are appropriate for a slab ML, they cannot capture the shear within the ML responsible for tilting isopycnals and increasing stratification as in OBS.

Equation (4) suggests that the evolution of shear will depend on the imbalance of the inertial terms (CORI + PRES) and friction (DIFF). These terms were evaluated in 2D using the time-integrated vertical derivatives of the momentum tendency terms (Fig. 5). During stage 2, the presence of friction (DIFF) produced shear that was positive across the front and against the geostrophic shear, while the inertial response (CORI + PRES) had a tendency to decrease the downgradient shear and reinforce the alongfront shear. During stage 3, winds rotated to the upfront position and input shear against the geostrophic flow.

The terms in Eqs. (4) were explored further using 1D+. The contribution from initial shear versus friction were evaluated by solving 1D+ for (i) all terms in Eqs. (4) (Figs. 6b,f), (ii) no turbulence (i.e., no DIFF; Figs. 6c,g), and (iii) no initial shear (Figs. 6d,h). The vertical structure of shear from 2D (Figs. 6a,e) and 1D+ (Figs. 6b,f) highlight the important role of the inertial response and friction. An oscillatory behavior existed deeper, indicative of waves (where only TEND and CORI dominate), while contributions from the horizontal buoyancy gradient
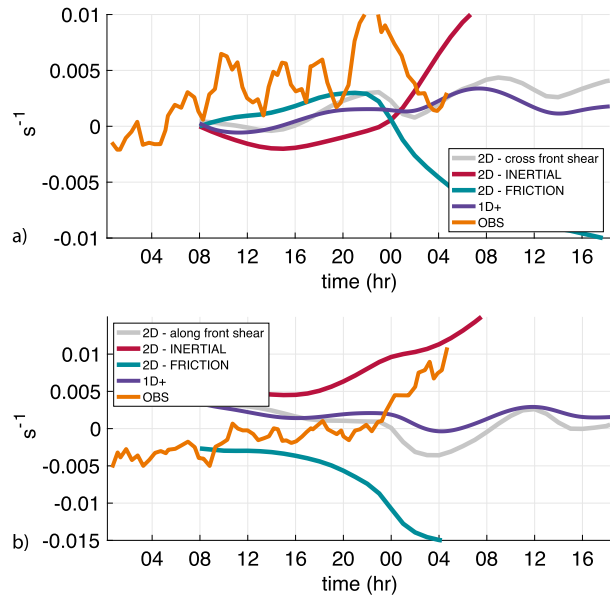
(PRES) and friction (DIFF) were seen near the surface and throughout the ML. The case of no turbulence (Figs. 6c,g) was similar to inviscid adjustment (TG94), where the time-dependent solution included inertial oscillations. Here, the solution was modified by thermal wind imbalance set by the remnant shear from previous days of wind forcing. This allowed for larger values and nonuniform shear within the ML compared to the classic adjustment problem (which had a maximum shear of $2M^4f^{-2}$, TG94). The absence of a damping term (by omitting friction, DIFF) implied the flow would continue as sheared inertial oscillations. This was not the case when considering turbulence and unsteady forcing (Figs. 6d,h). Momentum input at the surface combined with the redistribution of momentum by DIFF simultaneously damped the inertial oscillation and introduced an external source of shear, also larger than that of inviscid adjustment, particularly near the surface. The simplicity of Eq. (4) highlights the importance of the transient frontal response to thermal wind imbalance resulting from the initial shear and turbulence in the ML combined with unsteady wind forcing at the surface. These terms worked in concert to evolve the shear.

The evolution of shear in 2D was matched by the 1D+ solution, and deviations point to the importance of time-varying viscosity and higher-order terms in 2D (Wenegrat and McPhaden 2016; Dauhajre and McWilliams 2018). Nonetheless, 1D+ captures the structure of shear predicted by the more complex 2D during the time span of
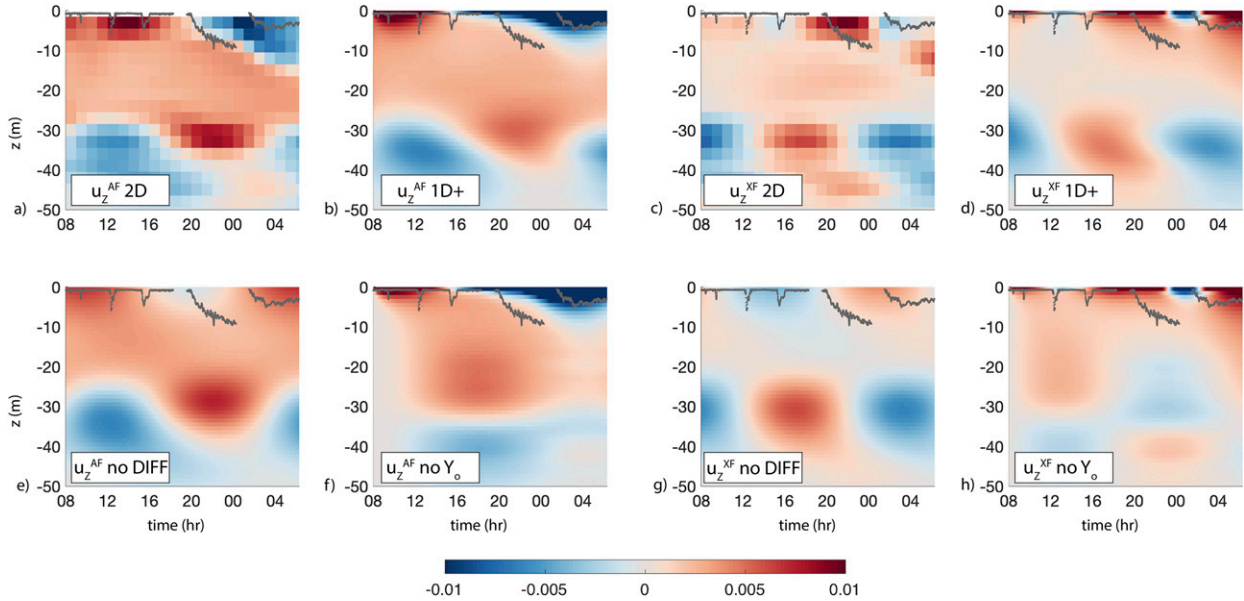
FIG. 6. (left),(left center) Alongfront and (right center),(right) cross-frontal shear predicted by (a),(c) 2D, (b),(d) 1D+, (e),(g) 1D+ without friction (no DIFF), and (f),(h) 1D+ without initial shear (no Y_o). Float depth from OBS (gray dots) is included for reference.

the observations and suggests these are the dominant terms modulating shear in the ML.

Model 1D+ was also solved with initial conditions determined from OBS. Triaxus data at yd 216.3 provided an initial condition for Y and M^2, while ν was taken as the cross-frontal averaged profile from 2D. The agreement between the 1D+ solution and OBS is less obvious (Fig. 7). This may be due to alongfront variability and curvature that influenced M^2, as well as the semi Lagrangian interpretation of the observations at depth (Part I). Within the pycnocline (50 m), the solution and observations exhibited similar oscillatory behavior, confirming that oscillations in the observations (that also appear in 2D) were NIO trapped below the ML. Yet near the surface, the agreement between 1D+ and OBS is more complicated (Figs. 7 and 5). Agreement in cross-frontal shear between OBS, 2D, and 1D+ suggests the influence of friction (DIFF) during the restratification phases stages 2 and 3. This was not the case in alongfront shear where OBS disagrees with 1D, 2D, and the friction term, but instead increases with the inertial terms (CORI + PRES). During stage 3, the model eroded the daytime near-surface stratification while the OBS withstood erosion and continued to stratify. This interaction between friction and stratification may explain part of the discrepancy between the shear in 2D and OBS and is discussed in section 4b.

The 1D+ framework is a simple reduced set of coupled equations that explained the evolution of shear at this wind forced front similar to 2D. Specifically,

1D+, 2D, and OBS all exhibited a positive cross-frontal shear (Fig. 5). It will be shown that this cross-frontal shear is able to differentially advect buoyancy across the front to enhance stratification comparable to the observations.

b. Stratification

The lack of an external strain field in 2D resulted in a weaker horizontal buoyancy gradient and therefore weaker vertical stratification than OBS. As such, the dominant source of stratification in 2D was from diurnal warming (as compared with only ~20% of near-surface stratification in OBS). To account for this discrepancy, the advective source of stratification in 1D+, 2D, and OBS were isolated. In section 4a, the frontal response to turbulence and thermal wind imbalance induced a shear that differentially advected buoyancy across the front and modified vertical stratification. In Part I, the amount of stratification from horizontal advection was estimated as

$$N^2_{\mathrm{ADV}} = \int_{t_o}^{t_i} -\frac{\partial b}{\partial x}\frac{\partial u}{\partial z} - \frac{\partial b}{\partial y}\frac{\partial v}{\partial z}\, dt. \qquad (8)$$

Here, N^2_{ADV} was solved for 1D+ with corresponding initial M^2, and for 2D at each grid point. N^2_{ADV} was also solved for the solution to TTW [$if Y = -M^2 + \partial^2(\nu Y)/\partial z^2$; Gula et al. 2014] and for inviscid adjustment ADJ ($\partial Y/\partial t = -if Y - M^2$; TG94) at every grid point and averaged across the front. Results were nondimensionalized
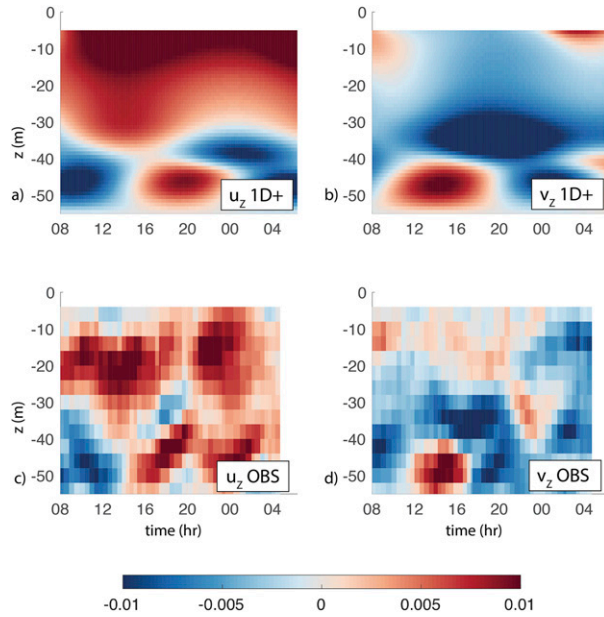
FIG. 7. Vertical shear predicted by 1D+ (initialized with OBS at the beginning of stage 2) compared with OBS. Only stages 2 and 3 are shown. Shown are (a) 1D+ zonal shear, (b) 1D+ meridional shear, (c) OBS zonal shear, and (d) OBS meridional shear.

FIG. 8. The N^2 (normalized to Ri_B) predicted by different models compared with the observations. The N^2 from OBS and N^2_{ADV} for the 1D+ solution to OBS are in dark green and light green, respectively. The N^2_{ADV} in 2D and the 1D+ solution to 2D are in dark purple and light purple, respectively. Also included are N^2_{ADV} from 1D+ solutions to ADJ (TEND, ADV, and PRES; orange) and TTW (ADV, PRES, and DIFF; yellow).

in terms of balanced Richardson number $\mathrm{Ri}_b = N^2 f^2 / M^4$, making comparison between the observations and 2D model simulations possible, since M^2 is almost an order of magnitude larger in OBS than in 2D. This also allows the results to be compared with the inviscid geostrophically adjusted state in TG94, where $N^2 = M^4/f^2$, and $\mathrm{Ri}_b = 1$ (Fig. 8).

The N^2_{ADV} from the 2D and the 1D+ solutions increased at rates similar to OBS, suggesting cross-frontal shear predicted by these idealized models were capable of reproducing the observed tilting of the front. If the evolution was inviscid, as in TG94, shear would tilt isopycnals over and retilt them back to vertical in an NIO. Conversely, if this was a case of TTW balance, the Ekman transport and TTW circulation would stratify weakly at a rate unrelated to the tendency in the model and observations.

The combination of terms encapsulated in Eq. (4) (TEND, CORI, PRES, and DIFF) suggest transient, super inertial pressure gradient and frictional effects were responsible for advecting horizontal stratification across the front. Without an external source of friction at the boundary, the ML shear due to ADJ would damp out as momentum is distributed evenly throughout the water column by friction. The surface boundary condition modified this further by providing an external input of shear. The instantaneous magnitude and direction of friction at
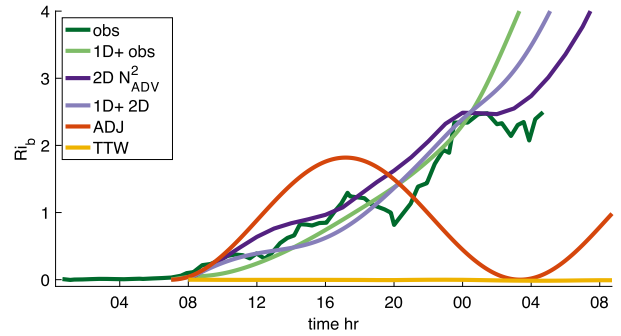
the surface was rotated as it was distributed throughout the turbulent boundary layer by the DIFF term via unsteady Ekman dynamics. This highlights the importance of friction and transience, both of which were needed to produce a persistent flattening of isopycnals. This differentiates this simple 1D+ model and the observations from traditional ADJ, slab ML NIO, or balanced TTW.

This section brought together a simple reduced model of turbulent adjustment with an idealized 2D numerical simulation to highlight the role of unsteady wind forcing on the evolution of a shallow ML front. Yet the difference in ∇b between OBS and 2D suggests the importance of external circulation and alongfront variability, which were excluded in the idealized representations of the front and play an important role on the frontal structure.

c. Potential vorticity

The role of different processes in setting the stratification can be seen through Ertel's form of PV:

$$q = (f\hat{\mathbf{z}} + \nabla \times \mathbf{u}) \cdot \nabla b. \qquad (9)$$

Neglecting the contribution from vertical velocity, this can be written as a sum of the vertical and horizontal components:

$$q_v = (f + \zeta)N^2 \quad \text{and} \qquad (10)$$

$$q_h = \frac{\partial u}{\partial z}\frac{\partial b}{\partial y} - \frac{\partial v}{\partial z}\frac{\partial b}{\partial x}. \qquad (11)$$

Part I evaluated q_v and q_h in OBS and found that changes in these terms balanced each other in the

middle of the ML (16 m), illustrating PV conservation. This was not the case near the surface (8 m) where q followed q_v as the near-surface stratified, while the contribution from q_h remained near zero. This increase of PV near the surface indicated the influence of PV injection on near-surface stratification.

Comparison of PV in 2D versus OBS is obscured by underestimation of $|\nabla_h b|$ in 2D which resulted in stratification dominated by heat flux rather than frontal tilting (Fig. 4). To account for this, PV was calculated from 2D at 8 m (as in Part I) using N^2_{ADV} to isolate the contribution of friction from that due to diabatic heating (Fig. 9). Downfront winds prior to the survey drove down PV in the ML (Thomas 2005), resulting in negative PV at 8 m before the survey and during stage 1. As wind forcing subsided, shear developed as a result of adjustment as well as momentum input at the surface that was redistributed in depth by friction (DIFF). The resulting cross-frontal shear advected buoyancy to increase N^2 and therefore PV through q_v. Note that cross-frontal shear did not impact q_h because the alongfront buoyancy gradient, by definition of the 2D model, was zero. Therefore alongfront shear was the only term that influenced PV through q_h. In 2D, q_h increased during stage 3, which was opposite of the observations (see Part I, their Fig. 14) where observed q_h remains negative throughout the survey. This disagreement may be traced to the difference in alongfront shear between OBS and 2D exhibited by the momentum budget terms (Fig. 5). This presents a discrepancy between the alongfront shear in 2D and OBS. Nonetheless, the role of DIFF in the redistribution of shear, and therefore in modulating q_h and q_v, confirms the importance of friction on near-surface PV.

5. Alongfront variability

Horizontal gradients observed in Part I increased in magnitude as smaller scales were resolved. For example, an external strain field induced by the mesoscale circulation was documented by an accompanying mesoscale survey Pallàs-Sanz et al. (2010b) and AVISO (Archiving, Validation, and Interpretation of Satellite Oceanographic Data; http://www.marine.copernicus.eu). This larger scale strain field was augmented by an internal strain field measured by OBS that modulated with a meandering buoyancy field. This alongfront variability was apparent throughout the observations and suggested by satellite SST (see Part I, their Fig. 1) that revealed wavelike structures along the front. Wavelike patterns have been studied in many high-resolution numerical simulations as frontal instabilities (e.g., Capet et al. 2008). Similar variability was captured by the Triaxus survey in Part I and
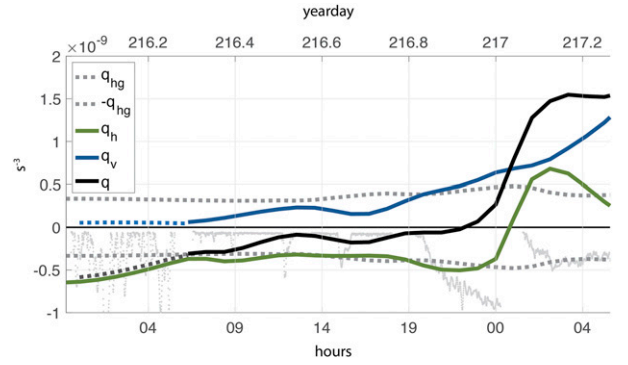

FIG. 9. The PV at 8 m from 2D using N^2_{ADV} to isolate changes resulting from vertical shear: total q (black), horizontal q_h (green) and vertical q_v (blue). Gray dashed lines are the PV associated with thermal wind balance $q_{hg} = -b^2_{\text{xf}}/f$. The observed float depth (scaled by a factor of 10^{-10}) is included for reference.

imprinted throughout fields of velocity, strain, vorticity and horizontal buoyancy gradient. Strong horizontal gradients, meanders, and vertical velocity are all features suggestive of growing baroclinic waves. In the ML, fronts exist in an environment of low stratification and high Rossby number. This makes them susceptible to a type of ageostrophic baroclinic instability (BCI; Stone 1966; Boccaletti et al. 2007). These instabilities grow into eddies, mixed layer eddies (MLE), that reach finite amplitude and stratification ensues. The rate of stratification from MLE has been parameterized as an overturning streamfunction for course resolution models (Fox-Kemper and Ferrari 2008; Fox-Kemper et al. 2008, 2011):

$$\Psi_o = C_e \frac{\nabla_h b H^2 \times \hat{\mathbf{z}}}{|f|} \mu(z), \tag{12}$$

$$\mu(z) = \left[1 - \left(\frac{2z}{H} + 1 \right)^2 \right] \left[1 + \frac{5}{21} \left(\frac{2z}{H} + 1 \right)^2 \right], \quad \text{and} \tag{13}$$

$$\frac{dN^2}{dt} = -C_e \frac{\nabla_h b^2 H^2}{|f|} \frac{\partial^2 \mu(z)}{\partial z^2}, \tag{14}$$

where C_e is a constant set to 0.06. A compelling feature of this parameterization is the vertical structure of the overturning streamfunction $\mu(z)$ [analogous to that predicted by Eady (1949)] that captures near-surface intensification of MLE induced stratification (Fig. 10). The N^2 predicted by this parameterization developed a strikingly similar vertical structure as the observations, questioning the possible role of mixed layer eddies as the source of stratification. Yet the parameterization is meant to represent the alongfront and across-front
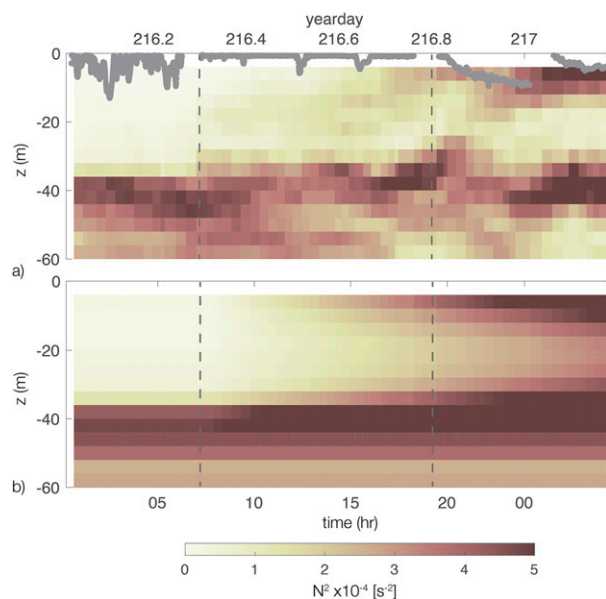
FIG. 10. Observed N^2 compared with that predicted by the MLE parameterization: (a) The N^2 from OBS in depth and time calculated from the Triaxus. Float position (gray dots) are included for reference. (b) The N^2 estimated from Eq. (14). Vertical gray dashed lines represent the division between stages.

averages within an idealized model, and not any instantaneous profile along the front. The OBS captured 5-km by 5-km averages of a ~1-km-wide front (e.g., Fig. 4) and did not necessarily average over a domain of vigorous eddies. Furthermore, the parameterization as represented here does not account for the external strain field or surface forcing, both of which modify the instability and frontal structure. While SST and in situ data suggest frontal instability at this upwelling front, the results from sections 4a and 4b demonstrate that adjustment modified by boundary layer turbulence was the mechanism driving the superinertial slumping of the front.

A major discrepancy between 2D and OBS was the lack of strain field in 2D that resulted in a broadening of the front compared with observations. Frontogenesis from baroclinic instability would influence the magnitude of the horizontal buoyancy gradient and therefore stratification resulting from the dynamics captured in Eq. (4).

Therefore, the 3D circulation magnifies the 2D effects described here. This brings attention to the importance of the external circulation and alongfront variability at enhancing stratification as observed. Additionally, the similarity in stratification predicted by MLE, the 2D model results (which inherently excludes MLE) and the observations confirm the difficulties in separating different processes at ML fronts and is discussed in section 7.

6. Buoyancy flux scalings

Many of the individual processes discussed throughout this paper have been identified as leading order in modulating stratification at fronts including the effect of wind-driven transport across a front [Ekman buoyancy flux (EBF); Thomas and Lee 2005], TTW (Wenegrat et al. 2018; McWilliams 2016), the transport of near-inertial oscillations across a front (NIO EBF; Savelyev et al. 2018), and MLE (Fox-Kemper and Ferrari 2008). These have been represented in the respective literature as an equivalent surface buoyancy flux $\mathscr{B}_{eq}$, which can be directly linked to the energetics of the system and the stratification. Scalings of $\mathscr{B}_{eq}$ were derived from a combination of theory and idealized modeling, and presented in observationally accessible state variables. This allows the restratifying/destratifying effects of these processes to be compared with each other and with surface heating/cooling. A brief description and associated $\mathscr{B}_{eq}$ are included in Table 1. A more in depth discussion can be found in (McWilliams 2016) and references in Table 1.

These scalings were calculated at this front using $\nabla_h b$, τ, from the observations, U_{NIO} from Eqs. (6) and (7), an $H = 30$ m and $\rho_o = 1024$ kg m^{-3} (Fig. 11). The value for MLE reach 3×10^{-6} m s^{-3}. TTW scaling derived in Wenegrat et al. (2018) follows the same parameter dependence as MLE (not shown). NIO EBF and surface heat flux (Q_{NET}) are orders of magnitude less at ~0.1×10^{-6} m s^{-3}. EBF suggests the importance of downfront winds in the beginning of the survey and upfront winds toward the end. Observed $\mathscr{B}_{eq}$ from Part I lies in between at 1×10^{-6} m s^{-3}. Though these values can be compared with each other, they do not provide

TABLE 1. Scalings of $w'b'$ for relevant processes shown to influence stratification at upper ocean fronts.

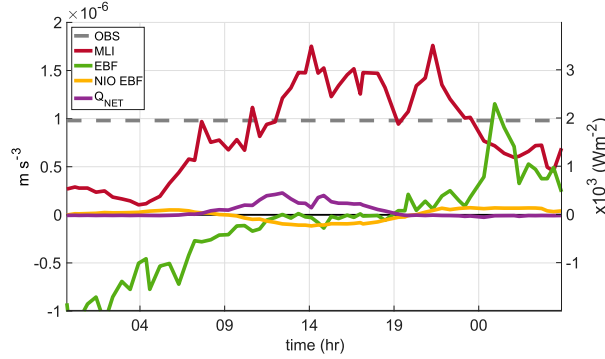|	$w'b'$	Description	Reference
Mixed layer eddies	$0.06\nabla_h b^2 H^2/f$	Baroclinic instability of a mixed layer front	Fox-Kemper et al. (2008)
Ekman buoyancy flux	$\tau \times \nabla_h b^2/(\rho f)$	Ekman transport across the front	Thomas and Lee (2005)
Near-inertial oscillation	$U_{NIO} \cdot \nabla_h b$	Near-inertial transport across the front	Savelyev et al. (2018)
Heat flux	$Q[\alpha g/(\rho c_p)]$	Vertical flux of buoyancy from heat at surface	—

FIG. 11. Scalings of $w'b'$ (left axis) and effective Q_{NET} (right axis) for MLI (red), EBF (green), NIO EBF (yellow), and observed Q_{NET} (purple). Values were calculated as in Table 1 using observed ∇b_h, H, f, τ, and solutions to Eqs. (6) and (7). Average $w'b'$ derived from the observed N^2 is included for reference (gray dashed line).

FIG. 12. Comparison between shear Richardson number Ri_s and horizontal buoyancy gradient $|\nabla b_h|$. The Ri_s was calculated during stage 3 (nighttime mixing) from OBS (green), from 2D (dark purple), and from the solution to 1D+ for varying M^2 (light purple). The dashed gray line corresponds to critical $Ri_s = 0.25$.

information about the likeliness of these dynamics occurring at this front. For example, these scalings are associated with processes that occur on different time and spatial scales that may not be appropriate for the localized nature of the observations and the rapid, superinertial evolution of stratification. For example, EBF and TTW assume subinertial time scales. Near-inertial oscillations describe the transport of a slab mixed layer, but do not necessarily capture the differential shear within the ML that may tilt a front over. MLE and TTW scalings were derived from a domain average over many fronts. Nonetheless, the observations and models reveal evidence of all of these processes (e.g., friction, inertial response, frontogenesis) occurring simultaneously to stratify the upper ocean rapidly within one inertial period.

7. Vertical structure of stratification

The external strain field was essential for strengthening ∇b and therefore the amount of N^2 by differential advection. This was evident when comparing the evolution of N^2 during stage 3 between OBS and 2D. The daytime N^2 in 2D was an order of magnitude less than OBS, and thus was not strong enough to resist erosion by nighttime mixing and convection. This was precisely when N^2 in OBS increased the most.

The absence of nighttime mixing in OBS during stage 3 highlights the importance of horizontal processes on the upper ocean buoyancy budget and reinforces the role of external and internal strain at influencing the strength of the front and therefore the magnitude of N^2. The relationship between horizontal buoyancy gradient and nighttime mixing was explored by solving 1D+ for a range of $|\nabla_h b|$. The resulting shear magnitude, $|\partial U/\partial z|$,
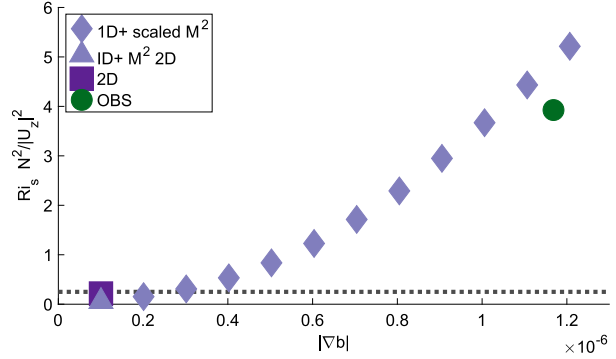
and N^2_{ADV} were used to estimate shear Richardson number $Ri_s = N^2/|\partial U/\partial z|^2$ during nighttime mixing (Fig. 12). The Ri_s in 2D was subcritical (i.e., $Ri_s < 0.25$), with $Ri_s = 0.05$, as compared with OBS, where $Ri_s = 4$. Stronger horizontal gradients increase N^2_{ADV} quadratically [through $\nabla_h b$ and $|\partial U/\partial z|$ via Eqs. (4) and (8)]. According to this metric, a buoyancy gradient of $\sim\nabla_h b = 2 \times 10^{-7}\,\mathrm{s}^{-2}$ (as compared with $\nabla_h b = 1.5 \times 10^{-6}\,\mathrm{s}^{-2}$ in OBS) would be strong enough to maintain $Ri_s > 0.25$ and keep the upper ocean stratified as in the observations. Therefore, the external 3D circulation is essential for amplifying the 2D effects on stratification.

The observed stratification had a unique vertical structure that was enhanced near the surface (Fig. 13). This vertical structure was replicated by N^2_{ADV} from 2D and 1D+, suggesting these idealized models were capturing differential advection by boundary layer turbulence enhanced near the surface. This structure of stratification was also inherent in the MLE parameterization in Eq. (14), which shared the same behavior near the surface. The near-surface enhancement of stratification in 2D and MLE is traced to the dependence of $\partial N^2/\partial t$ on $\partial^2\mu(z)/\partial z^2$ in (14) and $\partial^2\nu/\partial z^2$ in Eq. (4), which have similar vertical structures defined by Eq. (13) for $\mu(z)$ and the shape function for ν in the K-profile parameterization (KPP; Large et al. 1994). The shared character of stratification between the observations, theories, and models demonstrates the complicated nature of teasing apart lateral processes in shallow ML. The agreement in the vertical structure of stratification would be different in very deep ML, where MLE stratification would penetrate deeper (Mahadevan et al. 2012), while frictional dynamics would dominate near the boundary (Wenegrat et al. 2018).
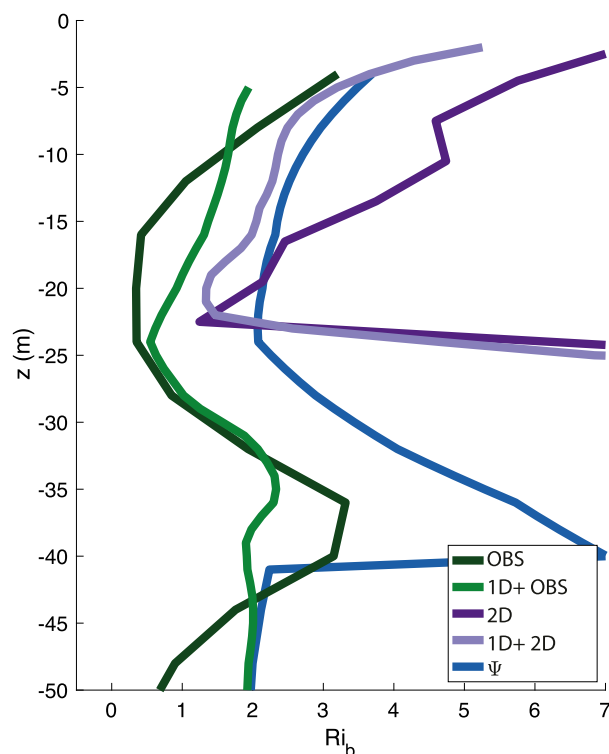
FIG. 13. Vertical structure of N^2 in terms of Ri_b predicted by different models compared with observations (e.g., see Figs. 8 and 10). The N^2 from OBS and N^2_{ADV} from 1D+ initiated with OBS are in dark green and light green, respectively. The N^2_{ADV} from 2D and 1D+ initiated with 2D are in dark purple and light purple, respectively. The N^2 predicted from MLI using Eq. (14) is in blue.

8. Discussion

This analysis describes the restratification of a front in the California Current System as a response to a sudden decrease in winds. Similarly, the work of Dale et al. (2008) detailed the rapid stratification of a shallow upwelling front after winds stopped and reversed direction. In that study, it was concluded that an imbalance in the cross-shelf pressure gradient resulted in a rapid on shore movement that steepened and slumped isopycnals simultaneously, therefore stratifying the ML on an inertial time scale. Dale et al. (2008) compared the rapid slumping of isopycnals to a gravity current, a process shown to occur at shallow ML fronts (i.e., Pham and Sarkar 2018). Furthermore, Dale et al. (2008) described the flow in context of NIO (TEND, CORI, DIFF) and adjustment, ADJ (TEND, PRES, CORI), but the combination of terms in Eq. (4) were not explored. In the set of observations described here, the flow resembled a near-inertial oscillation (i.e., section 4), yet it was the full solution to Eq. (4) that captured the shear within the ML needed to tilt the isopycnals over, highlighting the importance of frontal adjustment in the presence of

turbulence. As such, the initial shear in the ML when wind forcing stops along with the presence of BL turbulence created ML stratification exceeding that predicted by inviscid adjustment.

Dauhajre and McWilliams (2018) found two stages of frontogenesis in the T3W problem. The first stage documented the development of TTW by nighttime mixing due to winds and convection. The other stage documented was a convergence field that developed as the change in velocity (TEND) responded to the strength of horizontal buoyancy gradient (PRES) that changed across the front. The result was a pulse of convergence on an inertial time scale that occurred daily with the diurnal cycle (Dauhajre et al. 2017). This was similar to the mechanism explored by Dale et al. (2008) that suggested differential slumping of isopycnals sharpened the front as it tilted over. Both of these proposed mechanisms are consistent with the strengthening of the front seen in OBS as wind forcing stops, and is different than the frontolytic forcing implied by the deformation field in the generalized omega equation approach determined by a concurrent mesoscale survey (Pallàs-Sanz et al. 2010a). This presents a discrepancy between the temporal and spatial interpretation of this rapidly evolving front. The competing frontogenetic and frontolytic effects of BL turbulence (Gula et al. 2014; Bodner et al. 2019), advection (Dale et al. 2008; Dauhajre and McWilliams 2018), and external/internal strain (Hoskins and Bretherton 1972; Shakespeare and Taylor 2013; Barkan et al. 2019) play a key role in stratification at this front.

Furthermore, the surface stratification by differential advection converts horizontal changes of salinity and temperature into vertical ones on a time scale that competes with surface forcing. If the slumped gradients are subject to repeated mixing, they undergo a process of nonlinear diffusion (Young 1994) that leads to horizontal density compensation often observed in the ML (Rudnick 1999). This might provide a mechanism to homogenize the cold salty, recently upwelled waters with the warmer, fresher surface waters offshore, and therefore an important part in the mixing of tracers in the California Current System upwelling regime.

9. Conclusions

Detailed observations combined with idealized models show the importance of horizontal advection in stratifying the upper ocean. Specifically, an idealized 2D model combined with a simple reduced model, 1D+, were able to give insight into the role of turbulent adjustment that can rapidly stratify the ML on superinertial

time scales and compete with surface forcing. In addition, images of SST and alongfront variability captured in the observations suggest possible mixed layer instabilities, which grow on a relatively longer time scale, suggesting that this rapid stratification was dominated by turbulent adjustment.

The vertical structure of stratification reveals the importance of boundary layer dynamics on shallow ML fronts. Traditionally, attention has been given to the importance of fronts in deep MLs, as they have stored potential energy available to grow instabilities. Here demonstrates a mechanism of rapid restratification that can be dominant in shallow MLs and act to decrease the available potential energy faster than predicted from mixed layer baroclinic instability. This suggests the potential importance of shallow MLs on the upper ocean buoyancy budget (Johnson et al. 2016), where sharp fronts exist and therefore compensate for shallow ML depths.

None of the current scalings or parameterizations capture this rapid stratification (e.g., Table 1). NIO (Savelyev et al. 2018) has been used to explain the integrated Ekman transport of NIO over the deeper Gulf Stream, but does not provide information on shear within the boundary layer, which in this study is responsible for the stratification in OBS and 2D. EBF (Thomas and Lee 2005) and TTW (McWilliams et al. 2015; Wenegrat et al. 2018) demonstrate the importance of friction and viscosity on thermal wind balance, but assume subinertial time scales. In other words, the time-dependent adjustment is missing friction, and the friction scalings are not capturing transient shear due to unsteady winds. The observations combined with the model simulation presented here show that both are important for predicting the restratification at this shallow surface intensified front. The abundance of fronts in the upper ocean and the transience of surface forcing on the ML implies the dynamics explored here have implications for better representing fluxes of momentum, heat and gas exchange between the ocean and atmosphere.
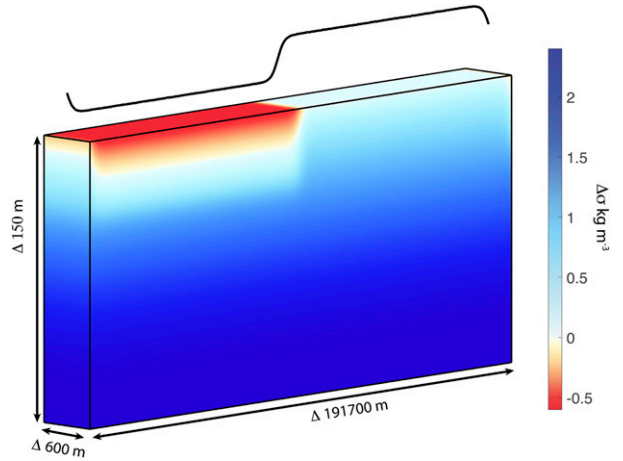
FIG. A1. Initial density structure in MITgcm. The alongfront distance is 600 m (2 grid points) with a cross-frontal direction of 191 700 m (639 grid points) and a horizontal resolution of 300 m. The vertical resolution was 3 m extending to 150-m depth. The cross-frontal density (scaled) is plotted above the front for visual reference. For an exact cross-frontal density structure, see Fig. 4.

APPENDIX

Configuration of the MITgcm

The MITgcm (Marshall et al. 1997) was run in hydrostatic mode with a horizontally periodic domain extending 600 m in the alongfront direction and 191 700 m across the front. The horizontal resolution was 300 m, allowing 2 grid points along the front and 639 grid points across the front. The vertical resolution was a uniform 3 m extending to 150 m depth. Horizontal mixing of momentum was parameterized using a biharmonic operator, with a Smagorinsky coefficient of 3, and Leith and modified Leith coefficients of 1. KPP was chosen for the vertical mixing scheme.

The model was initialized in the periodic domain using a geostrophically balanced double-front configuration, with a horizontal structure given by

$$Y(y) = \begin{cases} 0.5\left[1 - \tanh\left(\dfrac{y}{L_f}\right) + \tanh\left(\dfrac{y - L_y/2}{L_f}\right)\right]\left[\tanh\left(\dfrac{z + 2H}{H}\right) + 1\right], & 0 \le y \le L_y/2 \\ 0.5\left[\tanh\left(\dfrac{y - L_y/2}{L_f}\right) - \tanh\left(\dfrac{y - L_y}{L_f}\right) - 1\right]\left[\tanh\left(\dfrac{z + 2H}{H}\right) + 1\right], & L_y/2 \le y \le L_y \end{cases}.$$

This horizontal structure was then fit to the observed data to obtain a vertical structure using

$$T = \Delta T_o Y(y) + \Gamma_T(z) \quad \text{and}$$

$$S = -\Delta S_o Y(y) + \Gamma_S(z),$$

where $\Delta T_o = 1.6°C$, $\Delta S_o = 0.5\,\text{g kg}^{-1}$, and $\Gamma_T(z)$ and $\Gamma_S(z)$ were

$$\Gamma_T(z) = 0.4932 \exp\left(-8.466\,67 \times 10^{-6}\frac{z}{L_z}\right)$$
$$+ 0.5993 \exp\left(-1.7820 \times 10^{-4}\frac{z}{L_z}\right) \quad \text{and}$$

$$\Gamma_S(z) = 0.0710 \exp\left(-5.5373 \times 10^{-5}\frac{z}{L_z}\right)$$
$$+ 1.0980 \exp\left(-3.1193 \times 10^{-7}\frac{z}{L_z}\right).$$

Density was calculated assuming a linear equation of state $\rho = \rho_o + \rho_o[-\alpha_T(T - T_o) + \beta(S - S_o)]$, with $\alpha = 2.1766 \times 10^{-4}\,\text{K}^{-1}$, $\beta = 7.4137 \times 10^{-4}\,\text{kg g}^{-1}$, $T_o = 15.8°C$, and $S_o = 33.1\,\text{g kg}^{-1}$. The initial model domain can be seen in Fig. A1. Although the MITgcm configuration contained three dimensions, the use of only two grid point in the alongfront direction prevents alongfront variability while allowing cross-frontal variability. It was therefore interpreted as a 2D configuration.

REFERENCES

Barkan, R., M. J. Molemaker, K. Srinivasan, J. C. McWilliams, and E. A. D'Asaro, 2019: The role of horizontal divergence in submesoscale frontogenesis. *J. Phys. Oceanogr.*, **49**, 1593–1618, https://doi.org/10.1175/JPO-D-18-0162.1.

Boccaletti, G., R. Ferrari, and B. Fox-Kemper, 2007: Mixed layer instabilities and restratification. *J. Phys. Oceanogr.*, **37**, 2228–2250, https://doi.org/10.1175/JPO3101.1.

Bodner, A. S., B. Fox-Kemper, L. P. Van Roekel, J. C. McWilliams, and P. P. Sullivan, 2019: A perturbation approach to understanding the effects of turbulence on frontogenesis. *J. Fluid Mech.*, **883**, A25, https://doi.org/10.1017/jfm.2019.804.

Capet, X., J. C. McWilliams, M. J. Molemaker, and A. F. Shchepetkin, 2008: Mesoscale to submesoscale transition in the California Current System. Part I: Flow structure, eddy flux, and observational tests. *J. Phys. Oceanogr.*, **38**, 29–43, https://doi.org/10.1175/2007JPO3671.1.

Cronin, M. F., and W. S. Kessler, 2009: Near-surface shear flow in the tropical Pacific cold tongue front. *J. Phys. Oceanogr.*, **39**, 1200–1215, https://doi.org/10.1175/2008JPO4064.1.

Dale, A. C., J. A. Barth, M. D. Levine, and J. A. Austin, 2008: Observations of mixed layer restratification by onshore surface transport following wind reversal in a coastal upwelling region. *J. Geophys. Res.*, **113**, C01010, https://doi.org/10.1029/2007JC004128.

Dauhajre, D. P., and J. C. McWilliams, 2018: Diurnal evolution of submesoscale front and filament circulations. *J. Phys. Oceanogr.*, **48**, 2343–2361, https://doi.org/10.1175/JPO-D-18-0143.1.

——, ——, and Y. Uchiyama, 2017: Submesoscale coherent structures on the continental shelf. *J. Phys. Oceanogr.*, **47**, 2949–2976, https://doi.org/10.1175/JPO-D-16-0270.1.

Eady, E. T., 1949: Long waves and cyclone waves. *Tellus*, **1**, 33–52, https://doi.org/10.3402/tellusa.v1i3.8507.

Farrar, J. T., C. J. Zappa, R. A. Weller, and A. T. Jessup, 2007: Sea surface temperature signatures of oceanic internal waves in low winds. *J. Geophys. Res.*, **112**, C06014, https://doi.org/10.1029/2006JC003947.

Fox-Kemper, B., and R. Ferrari, 2008: Parameterization of mixed layer eddies. Part II: Prognosis and impact. *J. Phys. Oceanogr.*, **38**, 1166–1179, https://doi.org/10.1175/2007JPO3788.1.

——, ——, and R. Hallberg, 2008: Parameterization of mixed layer eddies. Part I: Theory and diagnosis. *J. Phys. Oceanogr.*, **38**, 1145–1165, https://doi.org/10.1175/2007JPO3792.1.

——, and Coauthors, 2011: Parameterization of mixed layer eddies. III: Implementation and impact in global ocean climate simulations. *Ocean Modell.*, **39**, 61–78, https://doi.org/10.1016/j.ocemod.2010.09.002.

Gula, J., M. J. Molemaker, and J. C. McWilliams, 2014: Submesoscale cold filaments in the Gulf Stream. *J. Phys. Oceanogr.*, **44**, 2617–2643, https://doi.org/10.1175/JPO-D-14-0029.1.

Hosegood, P., M. C. Gregg, and M. H. Alford, 2006: Sub-mesoscale lateral density structure in the oceanic surface mixed layer. *Geophys. Res. Lett.*, **33**, L22604, https://doi.org/10.1029/2006GL026797.

Hoskins, B. J., and F. P. Bretherton, 1972: Atmospheric frontogenesis models: Mathematical formulation and solution. *J. Atmos. Sci.*, **29**, 11–37, https://doi.org/10.1175/1520-0469(1972)029<0011:AFMMFA>2.0.CO;2.

Johnson, L., C. M. Lee, and E. A. D'Asaro, 2016: Global estimates of lateral springtime restratification. *J. Phys. Oceanogr.*, **46**, 1555–1573, https://doi.org/10.1175/JPO-D-15-0163.1.

——, ——, ——, L. Thomas, and A. Shcherbina, 2020: Restratification at a California Current upwelling front. Part I: Observations. *J. Phys. Oceanogr.*, **50**, 1455–1472, https://doi.org/10.1175/JPO-D-19-0203.1.

Large, W. G., J. C. McWilliams, and S. C. Doney, 1994: Oceanic vertical mixing: A review and a model with a nonlocal boundary layer parameterization. *Rev. Geophys.*, **32**, 363–403, https://doi.org/10.1029/94RG01872.

LeVeque, R. J., 2007: *Finite Difference Methods for Ordinary and Partial Differential Equations, Steady State and Time Dependent Problems*. Society for Industrial and Applied Mathematics, 184 pp.

Lévy, M., P. Klein, A.-M. Tréguier, D. Iovino, G. Madec, S. Masson, and K. Takahashi, 2010: Modifications of gyre circulation by sub-mesoscale physics. *Ocean Modell.*, **34**, 1–15, https://doi.org/10.1016/j.ocemod.2010.04.001.

Mahadevan, A., E. D'Asaro, C. Lee, and M. J. Perry, 2012: Eddy-driven stratification initiates North Atlantic spring phytoplankton blooms. *Science*, **337**, 54–58, https://doi.org/10.1126/science.1218740.

Marshall, J., A. Adcroft, C. Hill, L. Perelman, and C. Heisey, 1997: A finite-volume, incompressible Navier Stokes model for studies of the ocean on parallel computers. *J. Geophys. Res.*, **102**, 5753–5766, https://doi.org/10.1029/96JC02775.

McWilliams, J. C., 2016: Submesoscale currents in the ocean. *Proc. Roy. Soc.*, **472A**, 20160117, https://doi.org/10.1098/rspa.2016.0117.

——, and E. Huckle, 2006: Ekman layer rectification. *J. Phys. Oceanogr.*, **36**, 1646–1659, https://doi.org/10.1175/JPO2912.1.

——, J. Gula, M. J. Molemaker, L. Renault, and A. F. Shchepetkin, 2015: Filament frontogenesis by boundary layer turbulence. *J. Phys. Oceanogr.*, **45**, 1988–2005, https://doi.org/10.1175/JPO-D-14-0211.1.

Pallàs-Sanz, E., T. M. S. Johnston, and D. L. Rudnick, 2010a: Frontal dynamics in a California Current System shallow front: 1. Frontal processes and tracer structure. *J. Geophys. Res.*, **115**, C12067, https://doi.org/10.1029/2009JC006032.

——, ——, and ——, 2010b: Frontal dynamics in a California Current System shallow front: 2. Mesoscale vertical velocity. *J. Geophys. Res.*, **115**, C12068, https://doi.org/10.1029/2010JC006474.

Pham, H. T., and S. Sarkar, 2018: Ageostrophic secondary circulation at a submesoscale front and the formation of gravity currents. *J. Phys. Oceanogr.*, **48**, 2507–2529, https://doi.org/10.1175/JPO-D-17-0271.1.

Pollard, R., and R. Millard, 1970: Comparison between observed and simulated wind-generated inertial oscillations. *Deep-Sea Res. Oceanogr. Abstr.*, **17**, 813–821, https://doi.org/10.1016/0011-7471(70)90043-4.

Price, J. F., R. A. Weller, and R. Pinkel, 1986: Diurnal cycling: Observations and models of the upper ocean response to diurnal heating, cooling, and wind mixing. *J. Geophys. Res.*, **91**, 8411–8427, https://doi.org/10.1029/JC091iC07p08411.

Rudnick, D. L., 1999: Compensation of horizontal temperature and salinity gradients in the ocean mixed layer. *Science*, **283**, 526–529, https://doi.org/10.1126/science.283.5401.526.

Savelyev, I., and Coauthors, 2018: Aerial observations of symmetric instability at the North Wall of the Gulf Stream. *Geophys. Res. Lett.*, **45**, 236–244, https://doi.org/10.1002/2017GL075735.

Shakespeare, C. J., and J. R. Taylor, 2013: A generalized mathematical model of geostrophic adjustment and frontogenesis: Uniform potential vorticity. *J. Fluid Mech.*, **736**, 366–413, https://doi.org/10.1017/jfm.2013.526.

Stone, P. H., 1966: On non-geostrophic baroclinic stability. *J. Atmos. Sci.*, **23**, 390–400, https://doi.org/10.1175/1520-0469(1966)023<0390:ONGBS>2.0.CO;2.

Su, Z., J. Wang, P. Klein, A. F. Thompson, and D. Menemenlis, 2018: Ocean submesoscales as a key component of the global heat budget. *Nat. Commun.*, **9**, 775, https://doi.org/10.1038/s41467-018-02983-w.

Tandon, A., and C. Garrett, 1994: Mixed layer restratification due to a horizontal density gradient. *J. Phys. Oceanogr.*, **24**, 1419–1424, https://doi.org/10.1175/1520-0485(1994)024<1419:MLRDTA>2.0.CO;2.

Thomas, L. N., 2005: Destruction of potential vorticity by winds. *J. Phys. Oceanogr.*, **35**, 2457–2466, https://doi.org/10.1175/JPO2830.1.

——, and C. M. Lee, 2005: Intensification of ocean fronts by downfront winds. *J. Phys. Oceanogr.*, **35**, 1086–1102, https://doi.org/10.1175/JPO2737.1.

Thompson, A. F., A. Lazar, C. Buckingham, A. C. Naveira Garabato, G. M. Damerell, and K. J. Heywood, 2016: Open-ocean submesoscale motions: A full seasonal cycle of mixed layer instabilities from gliders. *J. Phys. Oceanogr.*, **46**, 1285–1307, https://doi.org/10.1175/JPO-D-15-0170.1.

Timmermans, M.-L., and P. Winsor, 2013: Scales of horizontal density structure in the Chukchi Sea surface layer. *Cont. Shelf Res.*, **52**, 39–45, https://doi.org/10.1016/j.csr.2012.10.015.

Van de Wiel, B. J. H., A. F. Moene, G. J. Steeneveld, P. Baas, F. C. Bosveld, and A. A. M. Holtslag, 2010: A conceptual view on inertial oscillations and nocturnal low-level jets. *J. Atmos. Sci.*, **67**, 2679–2689, https://doi.org/10.1175/2010JAS3289.1.

Wenegrat, J. O., and M. J. McPhaden, 2016: Wind, waves, and fronts: Frictional effects in a generalized Ekman model. *J. Phys. Oceanogr.*, **46**, 371–394, https://doi.org/10.1175/JPO-D-15-0162.1.

——, L. N. Thomas, J. Gula, and J. C. McWilliams, 2018: Effects of the submesoscale on the potential vorticity budget of ocean mode waters. *J. Phys. Oceanogr.*, **48**, 2141–2165, https://doi.org/10.1175/JPO-D-17-0219.1.

Young, W. R., 1994: The subinertial mixed layer approximation. *J. Phys. Oceanogr.*, **24**, 1812–1826, https://doi.org/10.1175/1520-0485(1994)024<1812:TSMLA>2.0.CO;2.